1

Corrosion of calcite crystals by metal-rich mud in caves: study case in *Crovassa Ricchi in Argento* Cave (SW Sardinia, Italy)

Fernando Gázquez[1,2*], José-María Calaforra[2], Paolo Forti[3], Jo De Waele[3], Laura Sanna[4], Fernando Rull[1,5], Aurelio Sanz[1]

[1]Unidad Asociada UVA-CSIC al Centro de Astrobiología, University of Valladolid. Parque tecnológico Boecillo, 47151. Valladolid (Spain) (f.gazquez@ual.es, rull@fmc.uva.es, jausanz@gmail.com)

[2]Water Resources and Environmental Geology Research Group, University of Almería, Crta.Sacramento s/n, 04120 La Cañada de San Urbano, Almería, Spain (jmcalaforra@ual.es)

[3]Italian Institute of Speleology, Department of Biological, Geological and Environmental Sciences, University of Bologna. Via Zamboni, 67, 40126. Bologna, Italy (paolo.forti@unibo.it, jo.dewaele@unibo.it)

[4]Dipartimentpo di Scienze della Natura e del Territorio. Università degli Studi di Sassari, Via Piandanna 4, 07100 Sassari, Italia (speleokikers@tiscali.it)

[5]Centro de Astrobiología (CSIC-INTA). Crta. Ajalvir, 28850. Torrejón de Ardoz, Madrid (Spain)

*Corresponding author

ABSTRACT

Unusual orange ocher crusts were recently discovered in *Crovassa Ricchi in Argento* Cave (San Giovanni Mine, SW Sardinia). These speleothems appear covering the cave walls on hydrothermal calcite spars as well as filling widened spaces between calcite crystals. Planar crusts display geometrical forms following the boundaries between the calcite spars, resembling a "mosaic".

32   EDX-SEM microanalyses reveal that these deposits comprise substances of

33   iron, manganese, lead, zinc, and oxygen that occur as solid inclusion in pits on

34   the surface of altered calcite microcrystals. Micro-Raman spectroscopy

35   analyses suggest the presence of calcite and ferromanganese oxides with low

36   degree of crystallinity. The genetic mechanism proposed for these speleothems

37   describes an initial stage of precipitation of euhedral calcite crystals from

38   thermal water under subaqueous conditions, as also observed in other nearby

39   mine caves of the Mt. San Giovanni Mine. The crystal surfaces were eroded

40   and corroded by colder aggressive water that smoothed the surfaces of the

41   crystals and slightly widened the spaces between calcite spars. Metal-rich mud

42   coming from alteration of bedrock and ore bodies filled the cave, also

43   penetrating along the spaces between the calcite spars. When the water table

44   fell below the cave level, part of the sediments was eroded but the cave walls

45   remained covered with metal-rich clayey sediments. Under aerobic conditions,

46   metals - which were reduced in previous stages - oxidized to oxides, lowering

47   the pH thus the crystal surface and the calcite planes between the spars were

48   corroded. Subsequently, the polymetallic crusts became harder through

49   evaporation occurring in the cave, "fossilizing" the products of this process

50   within the crystalline planes between the calcite spars. Finally, the exposed

51   calcite surfaces continued to be altered due to CO_2 diffusion into condensation

52   water, while the boundaries between crystals were preserved against corrosion

53   thank to the crust coating. As a result, the external crystal edges protrude by

54   several centimeters from the current cave wall, whilst the crystal surface are

55   depressed giving rise to calcite "ghosts".

56

1. Introduction

Metallic oxyhydroxides are the third group of cave minerals in abundance in caves, after carbonates and sulfates. Among them, iron and manganese minerals are undoubtedly the most common (Hill and Forti, 1997; Onac and Forti, 2011).
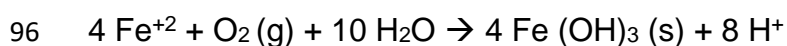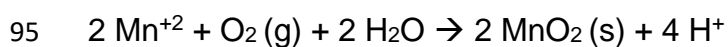
The morphology of ferromanganese speleothems in caves varies from layered black smooth crusts on the walls and the ceiling of caves (Kashima, 1983; White et al., 2009; Gázquez et al., 2011) to rough coatings on the cave walls, usually on top of visibly altered carbonate substrates (Northup et al., 2003; Spilde et al., 2005, 2006; Gázquez et al., 2012a). Rarely, ferromanganese substances have a plastic texture similar to a gel (Onac et al., 1997) and more frequently have been reported to form dripstones (Hill and Forti, 1997; Galán et al., 2011), intercalated with carbonate layers inside flowstones (Peck, 1986; Provencio and Polyak, 2001; Yusta et al., 2009; Gázquez et al., 2011), as solid inclusions inside hydrothermal gypsum speleothems (Gázquez et al., 2012b), in the bed of subterranean streams covering fluvial pebbles (Onac et al., 1997) or even forming cave pearls (Hill and Forti, 1997).

Manganese and iron coatings have usually been viewed as corrosion residues resulting from *in situ* weathering of the carbonate host rock (Kashima, 1983; Hill, 1987). Nevertheless, metals transported by subterranean streams (Onac et al., 1997), dissolution of the carbonate bedrock in the vadose zone overlying the cave (Spilde et al., 2005; Gázquez et al., 2012a) or mobilization of these metals

83   from mineralizations of the host rock under phreatic and anoxic conditions

84   (Gázquez et al., 2011) have been proposed as a further source of iron and

85   manganese in speleothems.

86   It is broadly accepted that fixation of some of these metals in caves is a

87   microbially-mediated process (Boston et al., 2001; Spilde et al., 2005; Rossi et

88   al., 2010; Yusta et al., 2010; Miller et al., 2012). Such assertion is particularly

89   true for manganese, which oxidation from Mn(II) to Mn(III) and Mn(IV) is largely

90   inhibited at low temperature in absence of microbial mediation (Calvert and

91   Pedersen, 1996; Jürgensen et al., 2004).

92   Oxidation of iron and manganese from their reduced forms in aqueous and oxic

93   conditions is a H^+-producing mechanism that gives rise to acidification following

94   the reactions:

95     $2\ Mn^{+2} + O_2\ (g) + 2\ H_2O \rightarrow 2\ MnO_2\ (s) + 4\ H^+$

96     $4\ Fe^{+2} + O_2\ (g) + 10\ H_2O \rightarrow 4\ Fe\ (OH)_3\ (s) + 8\ H^+$

97

98   In addition, microbial activity generates extracellular polymeric substances

99   (EPS) and metabolites with acid functional groups, usually accentuating the pH

100   lowering due to metal oxidation. At low pH, bacterial cell walls have negative

101   charges due to deprotonation of the organic functional groups, which may act

102   as nucleation sites for the aqueous metal cations such as iron and manganese

103   (Fein, 2000).

104   The effect of acidification produced by precipitation of ferromanganese oxides

105   on the carbonate substrate has been studied in a few hypogenic caves such as

106   those in the Guadalupe Mountains (New Mexico) (Hill, 1987; Spilde et al., 2006)

107   and Sima de la Higuera Cave (SE, Spain) (Gázquez et al., 2012a).

108 The present work studies the mechanisms of hydrothermal calcite crystals

109 corrosion due to metal oxidation in the muddy environment of the *Crovassa*

110 *Ricchi in Argento* Cave (Mining district of Iglesias, SW Sardinia, Italy). Such

111 mechanism gave rise to unusual orange ocher crusts resembling a mosaic,

112 which origin is the subject of the present study.

113

114 **2. Geological setting**

115

116 The San Giovanni Mine is located in the Iglesiente Mining District (South-West

117 Sardinia). Mining activities exploited lead, zinc and silver polymetallic sulfide

118 orebodies for more than 2,000 years in this area, though the mineral extraction

119 intensified since the middle of the XIXth century until late 1980s (Bechstadt and

120 Boni, 1996). In the Mt. San Giovanni, more than 50 natural caves with no

121 natural known entrance have been accidentally discovered when the mining

122 galleries intercepted them. The access to these caves is only possible via the

123 mine voids (Messina et al., 2005).

124 The regional geology comprises sedimentary materials deposited from Lower

125 Cambrian to Upper Carboniferous (Fig. 1), whereas the Mt. San Giovanni

126 orebodies are of Late Cambrian-Lower Ordovician age (Boni and Crescenzi,

127 1988).

128 Mt. San Giovanni is located on the southern slope of the San Giorgio Valley,

129 and forms an elongated NE-SW trending ridge. It represents the southern limb

130 of the Iglesias syncline (Civita et al., 1983), characterized by the Cambrian

131 carbonate succession, known as the Gonnesa Group (Bechstadt and Boni,

132 1996), in which the natural, mostly hypogenic caves in this area are developed.

The carbonate depositional sequence is composed, from bottom to top of: the Santa Barbara Formation consisting of "*Dolomia rigata*", grey dolostones with clear sedimentary structures, the San Giovanni Formation, characterized by a darker massive dolostone known as "*Dolomia grigia*" and a whitish-grey intensely karstified limestone known as "*Calcare ceroide*".

The basement of the carbonate sequence comprises meta-sandstones and phyllites of Lower Cambrian age (Nebida Group). Finally on top of the carbonate sequence there are nodular limestones and phyllites respectively of the Campo Pisano and Cabitza Formations (Middle Cambrian-Lower Ordovician), which represent the core of the Iglesias syncline (Bechstadt and Boni, 1996) (Fig. 1).

The climate of the area is of Mediterranean type, with hot and dry summers and relatively wet winters and autumns. Average air temperature in the caves of Mt. San Giovanni is around 15.5ºC (Chiesi, 2005).

Research in the mine caves of this area has mainly been carried out in the Santa Barbara Cave, whose complex mineralogy and evolution have been recently described by Pagliara et al. (2010). Moreover, a general study on the speleogenesis of the Mt. San Giovanni sulfuric acid caves, focusing not only on the Santa Barbara cave system but on a wide number of caves, has been published very recently (De Waele et al., 2013). Other recent work has studied the mineralogy and the geochemistry of blue aragonite flowstones from *Crovassa Azzurra* Cave (Caddeo et al., 2011), located nearby *Crovassa Ricchi in Argento* Cave which is subject of the current work.

Crovassa Ricchi in Argento Cave (silver-rich Cave) was accidentally intercepted by the Idina Gallery of the San Giovanni Mine in 1999 (Messina et al., 2005).

158 This cavity represents the basal level of the "Grotta Grande" mining quarter, the

159 surface entrance of which is located at 370 m a.s.l. The Idina Gallery is a

160 horizontal tunnel that develops along the 220 m level and extracted polymetallic

161 sulfides (i.e. galena and sphalerite) enriched in silver. The access to the cavity

162 from the mine excavations is ascending the side of a red clay accumulation, up

163 to 10 m high. The upper part of the clayey deposits is covered by a stalagmitic

164 pavement that constitutes the floor of a large chamber, 100 m in length and up

165 to 10 m in height. The entire cave develops between 210 m and up to 250 m

166 a.s.l (Fig. 1).

167 A small perched lake lies on the floor of the intermediate level of the cave. The

168 ceiling of this part of the chamber is covered by dark-colored soft crusts made

169 up of corrosion residues. Stalactites and stalagmites appear around this lake in

170 addition to white crusts (composed of micritized calcite) covering the cave walls

171 and speleothems.

172 The access to the upper part of the chamber is ascending a slope over an

173 accumulation of consolidated clayey sediments; the path is near the eastern

174 cave wall. Along this wall and in the upper part of the chamber are located the

175 corroded calcite crystal formations subject of this study.

176

177 **3. Methods**

178

179 **3.1 Description of the samples**

180

181 Two samples of the orange ochre crust that appears on the walls of the upper

182 part of the *Crovassa Ricchi in Argento* Cave (Fig. 1) were collected (GRA-03

183 and GRA-04) from two different zones along the wall. These crusts occur as

184 planar hard coatings covering the boundaries between calcite spars, giving rise

185 to a wall that resembles a "mosaic" of calcite crystals (Fig. 2A, B). Although

186 these crusts are consolidated and hard, up to 500 mg of powdered and grained

187 materials were easily taken from the wall by means of a metal scraper. The

188 same ochre materials also appear filling the spaces between euhedral calcite

189 crystals, some of them decimetric in size and showing smooth surfaces (Fig.

190 2C).

191 In addition, a sample of reddish clayey materials covering the lower part of the

192 wall was collected and labeled as GRA-02. Such unconsolidated detrital

193 deposits cover the walls up to one meter from the cave floor.

194

195 **3.2. Analytical methodology**

196

197 SEM microphotographs of samples GRA-03 and GRA-04 were taken using a

198 HITACHI S-3500 instrument in high vacuum mode. The sample was previously

199 dried and coated with graphite to increase electron transmissivity. The

200 elemental chemistry was determined by EDX (Energy Dispersive X-ray

201 spectroscopy) microprobe at five points with different typology over several

202 grains of the samples. Semiquantitative EDX microanalyses used the same

203 instrument coupled to an Oxford INCA 7210 X-ray detector, using a voltage of

204 20 kV. The diameter of the beam was approximately 1 µm. The limit of detection

205 of this technique enables major elements such as Fe, Mn, O, Si, Al, Ca, Pb, Zn,

206 and Ba to be analyzed. SEM and EDX analyses were performed at the

207 Technical Services Area of the University of Almeria (Spain).

208　The mineralogical nature of two clearly differentiated zones (dark spots and the

209　bright substrate) in samples GRA-03 and GRA-04 was also studied by *in situ*

210　micro-Raman spectroscopy. The excitation source was a Laser Research

211　Electro-Optics (REO) working at 632.8 nm. The spectrometer used was a KOSI

212　HoloSpec f/1.8i model from Kaiser, with Rayleigh scattering of 633 nm, a

213　spectral range of Raman displacement of 0-3800 cm^{-1} and spectral resolution of

214　5 cm^{-1}. The CCD used was a DV420A-OE-130 model from Andor working at -

215　40ºC, whereas the Raman head was a KOSI MKII, HFPH-FC-S-632.8 model

216　from Kaiser coupled by optical fibre. Microanalyses of up to 15 µm diameter

217　spots were undertaken with a Nikon Eclipse E600 microscope. The microscope

218　was coupled to the Raman probe and a JVC TK-C1381EG videocamera. For all

219　of the spectra, the laser power used on the sample was 1 mW, and the

220　irradiance, 1.9 kW/cm^2 at 100X. This ensures that no thermal damage affected

221　the samples. Acquisition time for each spectrum was 30 s and 8 accumulations

222　were done. The sample was manually scanned, while the height of focus was

223　varied in order to optimize the intensity of the spectra signals. The spectra

224　obtained were compared with the RRUFF Raman mineralogical database

225　standard (http://rruff.info/) for calcite and metallic oxyhydroxides and our own

226　database. Raman analyses were carried out at the Unidad Asociada UVA-CSIC

227　at the Centro de Astrobiología, University of Valladolid (Spain).

228　Quantitative chemical analysis of 1 g of clayey sediments (sample GRA-02) was

229　done using X-ray fluorescence (wavelength dispersive XRF) with a BRUKER S4

230　Pioneer instrument. XRF analyses were performed at the Technical Services

231　Area of the University of Almeria (Spain).

232

4. Results

Images taken by binocular microscope have revealed that the ochre colored crusts of the *Crovassa Ricchi in Argento* Cave (GRA-03 and GRA-04) are composed of altered calcite (determined using micro-Raman spectroscopy), containing dark inclusions (Fig. 3A). Our preliminary mineralogical analyses using X-ray diffraction only found calcite. On the other hand, a preliminary chemical qualitative analysis of sample GRA-03 revealed the presence of Fe and Mn, in addition to Ca.

The spectroscopic signal of five dark spots analyzed in the samples is that of ferromanganese oxides, with Raman bands between 200 and 700 cm^{-1} (Fig. 3B, C and D) (Mironova-Ulmanea et al., 2009; Jubb and Allen, 2010) that have also been observed in polymetallic oxide deposits from other caves (Gázquez et al., 2012a,b; Miller et al., 2012). Despite the low grade of crystallinity of these pollymetallic minerals, evidenced by the broad peaks in the spectra, the mineralogy of some of the analyzed spots could be identified. In particular, the Raman signal offered by some of them was good enough to allow goethite (FeO(OH)) to be identified in two spots (Fig. 3C), with bands at 637 cm^{-1} (Fe-O symmetric stretching), 546 cm^{-1} (Fe-OH asymmetric stretching), 474 cm^{-1} (Fe-OH asymmetric stretching), 392 cm^{-1} (Fe-O-Fe/-OH symmetric stretching), 295 cm^{-1} (Fe-OH symmetric bending) and 282 cm^{-1} (Fe-O symmetric stretching), in concordance with previous spectroscopic analyses on this mineral (de Faria et al., 1997). On the other hand, two points produced spectra typical of manganese oxides, showing signals at 670 cm^{-1}, 628 cm^{-1}, 533 cm^{-1}, 491 cm^{-1}, and 277 cm^{-1} (Fig. 3B, D), roughly coinciding with the typical Raman signal of

258   todorokite [$(Na,Ca,K,Ba,Sr)_{0.3-0.7}(Mn,Mg,Al)_6O_{12}\cdot 3.2\text{-}4.5H_2O$] (Julien et al., 2004;

259   Kim et al., 2003; Kim and Stair, 2004). Nevertheless, the presence of further

260   Mn-Zn-Pb phases cannot be ruled out, as revealed by the EDX microanalyses

261   (Table 1). In addition, the Raman spectrum of one of these spots shows a

262   further broad signal around 1568 cm^{-1} (Fig. 3D). Calcite matrix has been

263   confirmed also using this technique with Raman signals corresponding to

264   vibration of the CO_3 group, at around 1752 cm^{-1} ($2\upsilon_2$), 1087 cm^{-1} (υ_1), 1437 cm^{-1}

265   (υ_3) and 711 cm^{-1} (υ_4) (Rutt and Nicola, 1974) (Fig. 3A).

266   The SEM microphotographs allowed two visibly different zones to be broadly

267   identified (Fig. 4A). Particularly, microphotographs taken in BSE (BackScatter

268   Electron imagery) mode show that the dark polymetallic inclusions present a

269   lighter coloration compared to the underlying calcite crystals (Fig. 4A and C).

270   This fact suggests that the dark inclusions are composed of relatively heavier

271   elements than those comprising the calcite substrate.

272   Sub-millimetric elongated calcite crystals, which surfaces are highly altered, are

273   the substrate for polymetallic inclusions (Fig. 4B). In places, the oxides are

274   located in pits on the calcite crystal surfaces (Fig. 4C). Specifically, Fe-Mn

275   substances appear on the sub-planar surface of aggregated calcite crystals

276   (Fig. 4A), suggesting ferromanganese inclusions display preferentially in the

277   exfoliation planes of the large calcite spars.

278   Oxides appear as nanocrystal fiber aggregates up to 10 μm wide (Fig. 4D, E

279   and F) resembling crumpled tissue, which are typical morphologies of biogenic

280   Mn oxides (Spilde et al., 2005; Feng et al., 2010; Frierdich et al., 2011; Miller et

281   al., 2012). The chemical composition of the dark aggregates was determined by

282   EDX microprobe at four points. Moreover, the chemical composition of calcite

283   microcrystals was also analyzed by this technique (Table 1). High

284   concentrations of Fe and Mn were detected using EDX microanalysis, thus

285   corroborating the mineralogical nature of these aggregates. The points

286   analyzed over the nano-laminae structures (GRA-03a, GRA-03c, GRA-03d, and

287   GRA-03e) present Mn concentrations ranging between 6.8 and 24.4 wt.%

288   whereas Fe concentrations range between 8.0 and 27.1 wt.%. There were also

289   relatively high concentrations of elements not detected in the underlying calcite,

290   such as Pb (up to 11.9 wt.%) and Zn (up to 8.8 wt.%) in addition to traces of Ca

291   (up to 6.9 wt.%), Si (up to 3.8 wt.%) and Al (up to 0.7 wt.%). The Ca-carbonate

292   nature of the substrate has also been confirmed (GRA-03b). Deviation by 7

293   wt.% in carbon concentration with respect to the ideal calcite composition

294   comes from graphite metallization for SEM observation. Thus, most of the

295   carbon detected in the Fe-Mn aggregates (up to 13.4 wt.%) is a result of the

296   carbon coating.

297   The XRF of a bulk sample of the sediments appearing along the lower part of

298   the wall (GRA-02) revealed high concentrations of O (40.6 wt.%), Al (14.2

299   wt.%), and Si (18.4 wt.%), significant amounts of Fe (8.4 wt.%), Ba (3.8 wt.%),

300   K (2.9 wt.%), and Zn (1.1 wt.%), and in addition a great array of trace elements

301   below 0.5 wt.%, such as Mn, Pb, Mg, Cu, Ni, Na, Cr, and S, among others.

302

5. Discussion

304

305   Precipitation of large-sized euhedral calcite crystals has been reported to occur

306   from thermal water in a variety of caves (Onac, 1992; Dublyansky, 1995;

307   Lundberg et al., 2000; Palmer et al., 2009; Gázquez et al., 2012c; Otoničar,

308   2012). Calcite spars, usually showing scalenohedral and rhombohedral habit,

309   appear filling voids and fractures of the host rock, as geodes (Audra et al.,

310   2009), as well as exposed on the cave walls (Lundberg et al., 2000).

311   In *Crovassa Ricchi in Argento* Cave, transparent scalenohedral and

312   rhombohedral calcite crystals appear on the walls, particularly in the upper part

313   of the cave where the samples of this study have been taken. The presence of

314   large-size calcite crystals in this cave is not an isolated fact but is reported from

315   many natural cavities and mine galleries of the Iglesiente Mining district, for

316   instance the Phaff Cave (Masua Mine; Fig. 1) (De Waele et al., 2001; De Waele

317   and Forti, 2006), and other caves in the San Giovanni Mine such as *Crovassa*

318   *Azzurra* Cave, Santa Barbara Cave or Massa Riccardo Mine Cave, also

319   hypogenic in origin (De Waele et al., 2013). These earlier works demonstrated

320   that precipitation of this type of well-developed calcite crystals in the Santa

321   Barbara Cave system, located in the vicinity of *Crovassa Ricchi in Argento*

322   Cave, occurred at around 40ºC (De Vivo et al., 1987; Forti et al., 2005). Such

323   centimetric-size crystals precipitated in low thermal water in a very stable

324   environment and close to the saturation equilibrium of calcite over long periods

325   of time (Fig. 5A).

326   Later, the temperature of the hydrothermal system decreased and the cave was

327   gradually filled with colder water, probably as a result of an increasing input of

328   meteoric water to the aquifer. The colder and oxygenated water induced the

329   oxidation of the sulfide orebodies in the host rock, which caused a strong

330   acidification of the seeping waters. The tip of the crystals exposed to the cave

331   void was dissolved and corroded by the acidic solutions, and the cave walls

332   were smoothed (Fig. 5B). Simultaneously, the spaces between single crystals

333 were slightly widened by interstitial infiltration of undersaturated water that

334 dissolved/corroded the planes of the calcite crystals.

335 At the same time, dissolution of the carbonate host rock was also enhanced due

336 to water acidification. Consequently, fine detrital materials interbedded in the

337 carbonate sequence (mainly clay and silt) were decalcified and the insoluble

338 residues incorporated into the subterranean flow. Red mud deposits appear

339 abundantly in *Crovassa Ricchi in Argento* Cave, especially on the floor but also

340 as sediments covering the cave walls up to 1 meter from the floor in the upper

341 cave level. Under phreatic conditions, mobilization of reduced metallic ions like

342 Fe^{2+} and Mn^{+2} was possible, both from the marine carbonate host rock and

343 mainly from the polymetallic sulfide minerals of the host rock (Fig. 5C).

344 Also clay minerals can play an essential role in the transport of metals through

345 this karst system. Clays present a great capacity for exchanging cations with

346 the solution as well as for metal adsorption due to their large specific surface

347 (Basta and Tabatai, 1992). In fact, the XRF analysis of the sediment samples

348 from *Crovassa Ricchi in Argento* Cave revealed meaningful concentrations of

349 Fe, Zn, Mn, Pb, Cu, Cr, and Ni that represent over 10% of the whole sample

350 weight. During this stage, clay also penetrated into the widened space between

351 the calcite spars.

352 Subsequently, the water table fell and vadose oxidised conditions prevailed at

353 the cave level. In this new phase, most part of the detrital sediments was

354 removed and mobilized toward deeper levels of the karst. However, a layer of

355 clayey materials remained covering the cave walls and the ceiling and were

356 ultimately hardened due to evaporation (Fig. 5D).

357 Simultaneously, a first stage of oxidation of bivalent ions to trivalent/tetravalent

358 ions occurred, resulting in precipitation of oxides, mainly iron and manganese

359 minerals. As a result of low proportion of dark inclusions with respect to the

360 calcite matrix, XRD did not reveal these ferromanganese substances.

361 Nevertheless, micro-Raman spectroscopy enabled goethite and todorokite-like

362 oxides to be identified (Fig. 3B,C and D).

363 Although the SEM images did not show any clear evidence of active

364 microorganisms implicated in the oxidation of some metals, this process has

365 been demonstrated to be usually catalyzed by microorganisms, especially for

366 manganese (Calvert and Pedersen, 1996; Jürgensen et al., 2004). In fact, many

367 research works have focused on the role of microorganisms in the genesis of

368 ferromanganese oxides in caves (Peck, 1986; Provencio and Polyak, 2001;

369 Boston et al., 2001; Spilde et al., 2005; Rossi et al., 2010; Miller et al., 2012). In

370 support to this, the Raman spectra of some pollymetallic inclusions found in

371 these crusts show a broad signal around 1568 cm^{-1} (Fig. 3D) which is in the

372 range of the typical Raman signals coming from organic compounds, similar to

373 amorphous carbon (Reich and Thomsen, 2004), suggesting a possible

374 biological origin of these manganese substances.

375 In this case, ferromanganese minerals precipitated as aggregates like dark

376 inclusions along the space between single crystals, as well as along the

377 intracrystalline planes of the calcite spars. During this stage calcite was

378 corroded along the intracrystalline planes, by acid solutions generated by both

379 CO_2 diffusion into the solution and oxidation of iron and manganese. As

380 explained in the introduction section, oxidation of iron and manganese releases

381 protons and lowers the pH. This fact is supported by the arrangement of the Fe-

382 Mn aggregates on the calcite microcrystals observed by SEM (Fig. 4C), that

383 appear embedded in pockets on the surface of the calcite, suggesting that

384 oxidation of metals and precipitation of oxides led to the corrosion and alteration

385 of the calcite (Fig. 4C and E).

386 Subsequently, further diffusion of O_2 from the cave atmosphere to the

387 sediments led to the total oxidation of metals. The ferromanganese oxides and

388 the microcrystalline calcite resulted from corrosion, formed the visible ochre

389 hard crust that greatly inhibited the contact between the calcite and the cave

390 atmosphere, thus "fossilizing" the products of this process (Fig. 5E).

391 When the stage of oxidation was completed, the thin and incoherent layer of

392 dried oxides and microcrystals was easily removed and part of the surfaces of

393 the calcite crystals were exposed to the cave atmosphere. Nevertheless, the

394 oxides deposited within the widened space between the calcite spars were not

395 removed. Besides, evaporation produced dehydration of the crusts, so making

396 them harder and harder.

397 In a subsequent stage, water vapor condensed over the exposed calcite spar

398 faces and CO_2 diffusion from the cave atmosphere into the water induced

399 corrosion, thus creating depressions on the exposed crystal surfaces bordered

400 by the oxides crusts (Fig. 5E) and resulting in calcite "ghost" formation. The

401 solutions migrating by capillarity inside and over the protruding oxide deposits

402 and the subsequent evaporation partially cemented and hardened the crusts

403 even more. The oxides layer in contact with calcite became almost totally

404 impervious and therefore protected all the covered areas from further corrosion-

405 dissolution.

406

6. Conclusions

Our geochemical and mineralogical analyses have revealed that the orange ochre crusts with reticular forms appearing on euhedral calcite spars in *Crovassa Ricchi in Argento* Cave comprise calcite microcrystals, goethite and poorly crystalline Mn-Zn-Pb oxides.

The genetic mechanism proposed for these speleothems describes (1) a first stage of precipitation of calcite spar that took place in phreatic and low thermal conditions, covering the walls and the cave ceiling; and (2) a second phreatic phase in which colder and acid water of meteoric origin substituted the hydrothermal water and oxidized the sulfide orebodies of the host rock. Acid solutions led to corrosion of the crystal surfaces exposed to the cave void. Subsequently, (3) mud and metal-rich clayey sediments filled the cave, before (4) the water table fell and conditions became vadose and aerated, when reduced metals (mainly Fe^{2+} and Mn^{2+}) oxidized, giving rise to ferromanganese oxides. Later (5), when detrital sediments were removed, evaporation caused hardening of the crusts. Finally (6), the calcite crystal surfaces exposed to the cave environment were dissolved and corroded by condensation water, leaving in relief the typical ochre reticular crust.

442

6. References

444 Audra, Ph., Mocochain, L., Bigot, J.Y., Nobecourt, J.C., 2009. Hypogene cave

445   patterns, In: Klimchouk, A.B., Ford, D.C (Eds.), Hypogene Speleogenesis

446   and Karst Hydrogeology of Artesian Basins. Ukrainian Institute of Speleology

447   and Karstology, Simferopol, Special Paper 1, pp. 23-32.

448 Basta, N.T., Tabatai, M.A., 1992. Effect of cropping systems on adsorption of

449   metals by soils: single metal adsorption. Soil Science 153(2), 108-114.

450 Bechstadt, T., Boni, M., 1996. Sedimentological, stratigraphical and ore

451   deposits field guide of the autochtonous Cambro-Ordovician of Southwestern

452   Sardinia. Memorie descrittive della Carta Geologica d'Italia. 48, 1-390.

453 Boni, M., Crescenzi, E., 1988. Caratteri della mineralizzazione del Contatto

454   Ovest, "Miniera di San Giovanni" (Iglesias, Sardegna Sud-occidentale).

455   Rendiconti della Società Geologica Italiana 11, 93-96.

456   Boston, P.J, Spilde, M.N., Northup, D.E. Melim, L.A., Sorok, D.S., Kleina, L.G.,

457   Lavoie, K.H., Hose, L.D., Mallory, L.M., Dahm, C.N., Crossey, L. J., Schelble,

458   R.T., 2001. Cave Biosignature Suites: Microbes, Minerals, and Mars.

459   Astrobiology 1, 25-54.

460   Caddeo, G.A., De Waele, J., Frau, F., Railsback, L.B., 2011. Trace element and

461   stable isotope data from a flowstone in a natural cave of the mining district of

462   SW Sardinia (Italy): evidence for Zn^{2+} induced aragonite precipitation in

463   comparatively wet climatic conditions. International Journal of Speleology 40

464   (2), 181-190.

465   Calvert, S.E., Pedersen, T.F., 1996. Sedimentary geochemistry of manganese;

466   implications for the environment of formation of manganiferous black shales.

467   Economic Geology 91, 36-47.

468   Chiesi, M., 2005. Il pre-monitoraggio dei parametri ambientali della Grotta di

469   Santa Barbara (Miniera di San Giovanni, Iglesias). In: De Waele, J.,

470   Naseddu, A. (Eds.) Le Grotte di Miniera: tra economia mineraria ed

471   economia turistica. Memorie dell'Istituto Italiano di Speleologia 17, 23-34.

472   Civita, M., Cocozza, T., Forti, P., Perna, G., Turi, B., 1983. Idrogeologia del

473   bacino minerario dell'Iglesiente (Sardegna sud-occidentale). Memorie

474   dell'Istituto Italiano di Speleologia 2, 1-139.

475   De Faria, D.L.A., Silva, S.V., de Oliveira, M.T., 1997. Raman microspectroscopy

476   of some iron oxides and hydroxides. Journal of Raman Spectroscopy 28,

477   873-878.

478   De Vivo, B, Maiorani, A, Perna, G, Turi, B., 1987. Fluid inclusion and stable

479   isotope studies of calcite, quartz and barite from karstic caves in the Masua

480   Mine, southwestern Sardinia, Italy. Chemie der Erde-Geochemistry 46(3-4),

481   259-273.

482   De Waele, J., Forti, P., Perna, G., 2001. Hyperkarstic phenomena in the

483   Iglesiente mining district (SW-Sardinia). In: Cidu, A., (Ed.), Water-Rock

484   Interaction, Swets and Zeitlinger, Lisse, Netherlands, 619-622.

485   De Waele, J., Forti P., 2006. A new hypogean karst form: the oxidation vent.

486   Zeitschrift fur Geomorphologie 147, 107-127.

487   De Waele, J., Forti, P., Naseddu, A., 2013. Speleogenesis of a complex

488   example of an exhumed sulphuric acid karst in Cambrian carbonates (Mount

489   San Giovanni, Sardinia). Earth Surface Processes and Landforms, DOI:

490   10.1002/esp.3375.

491   Dublyansky, Y.V., 1995. Speleogenetic History of the Hungarian Hydrothermal

492   Karst. Environmental Geology 25(1), 24-35.

493   Fein, J.B., 2000. Quantifying the effects of bacteria on adsorption reactions in

494   waterrock systems. Chemical Geology 169, 265-280.

495   Feng, X.H., Zhu, M., Ginder-Vogel, M., Ni, C., Parikh, S.J., Sparks, D.L., 2010.

496   Formation of nano-crystalline todorokite from biogenic Mn oxides.

497   Geochimica et Cosmochimica Acta 74, 3232-3245.

498   Forti, P., Pagliara, A., Galli, E., Rossi, A., De Waele, J., Naseddu, A., Papinuto,

499   S., 2005. Studio morfologico e mineralogico di dettaglio del concrezionamen-

500   to del sistema carsico di Santa Barbara (Miniera di San Giovanni, Iglesias).

501   Memorie dell'Istituto Italiano di Speleologia 17, 57-68.

502 Frierdich, A.J., Hasenmueller, E.A., Catalano, J.G., 2011. Composition and

503   structure of nanocrystalline Fe and Mn oxide cave deposits: implications for

504   trace element mobility in karst systems. Chemical Geology 284, 82-96.

505 Frost, R.L., 2004. Raman spectroscopy of natural oxalates. Analytica Chimica

506   Acta 517, 207-214.

507 Galán, C., Nieto, M., Vera-Martín, C., 2011. Descubrimiento de espeleotemas y

508   depósitos estratificados de jacobsita en la Cueva Aixa. Sociedad de ciencias

509   Aranzadi. On line: http://www.cota0.com/wp-content/PDFS/jacobsita.pdf.

510 Gázquez, F., Calaforra, J.M., Forti, P., 2011. Black Mn-Fe Crusts as Markers of

511   Abrupt Palaeoenvironmental Changes in El Soplao Cave (Cantabria, Spain).

512   International Journal of Speleology 40(2), 163-169.

513 Gázquez, F., Calaforra, J.M., Rull, F. 2012a. Boxwork and ferromanganese

514   coatings in hypogenic caves: an example from Sima de la Higuera Cave

515   (Murcia, SE Spain). Geomorphology 177-178, 158-166.

516 Gázquez, F., Calaforra, J.M., Forti, P., Rull, F., Martínez-Frías, J., 2012b.

517   Gypsum-carbonate speleothems from Cueva de las Espadas (Naica mine,

518   Mexico): mineralogy and palaeohydrogeological implications. International

519   Journal of Speleology 41, 211-220.

520 Gázquez, F., Calaforra, J.M., Rull, F., Martínez-Frías, J., 2012c. Espeleotemas

521   y evidencias de cavernamiento hipogénico de la Sima de la Higuera (Pliego,

522   Murcia). In: Durán., J.J, Robledo, P., (Eds.), Las cuevas turísticas como

523   activos económicos: Conservación e innovación. Asociación española de

524   Cuevas turísticas. Madrid, pp. 21-34.

525 Hill, C.A., 1987. Geology of Carlsbad Cavern and other caves in the Guadalupe

526   Mountains, New Mexico and Texas: Socorro, NM. New Mexico Bureau of

527   Mines and Mineral Resources Bulletin 117, 150 p.

528 Hill, C.A., Forti, P., 1997. Cave minerals of the World (second edition). National

529   Speleological Society, Huntsville, 461 pp.

530 Jubb, A.M., Allen, C.A., 2010. Vibrational spectroscopic characterization of

531   hematite, maghemite, and magnetite thin films produced by vapor deposition.

532   ACS Applied Materials & Interfaces 2(10), 2804-2812.

533 Julien, C.M., Massot, M., Poinsignon, C., 2004. Lattice vibrations of manganese

534   oxides. Part I. Periodic structures. Spectrochimica Acta A 60, 689-700.

535 Jürgensen, A., Widmeyer, J.R., Gordon, R.A., Bendell-Young, L.I., Moore, M.M.

536   Crozier, E.D., 2004. The structure of the manganese oxide on the sheath of

537   the bacterium *Leptothrix discophora*: an XAFS study. American Mineralogist

538   89, 1110-1118.

539 Kashima, N., 1983. On the Wad-minerals from the cavern environment.

540   International Journal of Speleology 13, 67-72.

541 Kim, H-S, Pastén, P.A., Gaillard, J-F., Stair, P.C., 2003. Nanocrystalline

542   todorokite-like manganese oxide produced by bacterial catalysis. Journal of

543   the American Chemical Society 125, 14284-14285.

544 Kim, H-S., Stair, P.C., 2004. Bacterially produced manganese oxide and

545   todorokite: UV Raman spectroscopic comparison. The Journal of Physical

546   Chemistry B 108, 17019-17026.

547 Lundberg, J., Ford, D.C., Hill, C.A., 2000. A preliminary U-Pb date on cave spar,

548   Big Canyon, Guadalupe Mountains, New Mexico. Journal of Cave and Karst

549   Studies 62, 144-148.

550 Messina, M., Naseddu, A., Papinuto, S., Sanna, F., Sotgia, S., Forti, P., De

551   Waele, J., 2005. Le esplorazioni speleologiche della miniera di San Giovanni:

552   prime sintesi. In: De Waele, J., Naseddu, A., (Eds.), Le Grotte di Miniera: Tra

553   economia mineraria ed economia turistica. Memorie dell'Istituto Italiano di

554   Speleologia 17, 69-86.

555 Miller, A.Z., Dionísio, A., Sequeira-Braga, M.A., Hernández-Mariné, M., Afonso,

556   M.J., Muralha, V.S.F., Herrera, L.K., Raabe, J., Fernández-Cortés, A.,

557   Cuezva, S., Hermosin, B., Sanchez-Moral, S., Chaminé, H., Saiz-Jimenez, C.

558   2012. Biogenic Mn oxide minerals coating in a subsurface granite

559   environment. Chemical Geology 222-223, 181-191.

560 Mironova-Ulmanea, N., Kuzmina, A., Grube, M., 2009. Raman and infrared

561   spectromicroscopy of manganese oxides. Journal of Alloys and Compounds

562   480, 97-99.

563 Northup, D. E., Barns, S.M., Yu, L.E., Spilde, M.N., Schelble, R.T., Dano, K.E.,

564   Crossey, L.J., Connolly, C.A., Boston, J., Dahm, C.N., 2003. Diverse

565   microbial communities inhabiting ferromanganese deposist in Lechuguilla

566   and Spider Caves. Environmental Microbiology 5, 1071-1086.

567 Onac, B.P., 1992. Mineralogy of the Apuseni Mountains caves. Theoretical and

568   Applied Karstology 5, 193-201.

569 Onac, B.P., Pedersen, R.B., Tysseland, M., 1997. Presence of rare-earth

570   elements in black ferromanganese coating from Vântului cave (Romania).

571   Journal of Cave and Karst Studies 59, 128-131.

572 Onac, B.P., Forti, P., 2011. State of the art and challenges in cave minerals

573   studies. Studia UBB Geologia 56, 33-42.

574 Otoničar, B. 2012. Large calcite crystals from Cok Cave (abandoned Iron Mine),

575   Jelovica Plateau, NW Slovenia. Abstract Boo of the 2nd International

576   Congress on mine caves (Iglesias, Sardinia), 7-8.

577 Pagliara, A., De Waele, J., Forti, P., Galli, E., Rossi, A., 2010. Speleothems and

578   speleogenesis of the hypogenic Santa Barbara cave system (South-West

579   Sardinia, Italy). Acta Carsologica 39(3), 551-564.

580 Palmer, A.N., Palmer, M.V., Polyak, V., Asmerom, Y., 2009. Geologic history of

581   the Black Hills Caves, South Dakota, USA. In: White, W.B. (ed.) Proceedings

582   of the 15th International Congress of Speleology, Kerrville, Texas-USA, 2,

583   946-951.

584 Peck, S.B., 1986. Bacterial deposition of iron and manganese oxides in North

585   American caves. National Speleological Society Bulletin 48, 26-30.

586 Provencio, P.P., Polyak, V.J., 2001. Iron Oxide-Rock Filaments: Possible Fossil

587   Bacteria in Lechuguilla Cave, New Mexico. Geomicrobiology Journal 18, 297.

588 Reich, S., Thomsen, C., 2004. Raman spectroscopy of graphite. Philosophical

589   Transactions of the Royal Society of London A 362, 2271‑2288.

590 Rossi, C., Lozano, R.P., Isanta, N., Hellstrom, J., 2010. Manganese

591   stromatolites in caves: El Soplao (Cantabria). Geology 38, 1119-1122.

592 Rutt, H.N., Nicola J.H., 1974. Raman spectra of carbonates of calcite structure.

593   Journal of Physics C: Solid State Physics 7, 4522.

594 Spilde, M.N., Northup, D.E. Boston, P.J., Schelble, R.T., Dano, K.E., Crossey,

595   L.J., Dahm, C.N., 2005. Geomicrobiology of cave ferromanganese deposits:

596   A field and laboratory investigation. Geomicrobiology Journal 22, 99-116.

597 Spilde, M.N., Northup, D.E., Boston, P., 2006. Ferromanganese deposits in the

598   caves of the Guadalupe Mountains. New Mexico Geological Society

599   Guidebook, 57th Field Conference, Caves and Karst of Southeastern New

600   Mexico, pp. 161-166.

601 White, W.B., Vito, C., Scheetz, B.E., 2009. The mineralogy and trace element

602   chemistry of black manganese oxide deposits from caves. Journal of Cave

603   and Karst Studies 71, 136-143.

604 Yusta, I., Castellano, A., Aranburu, A., Velasco, F., 2009. Los depósitos de Mn-

605   Al-Fe de la Cueva de Lazalday (Zarate, Alava): composición química y

606   mineralogía. Geogaceta 47, 117-120.

607 Yusta, I., Sánchez-España, J., Castellano, A., Aranburu, A., Velasco, F., 2010.

608   Microestructuras en Espeleotemas de Mn-Al-Fe de la Cueva de Lazalday:

609   ¿Evidencias de un Origen Biogénico? Macla 13, 227-228.

610 Ruff Mineralogical database; http://rruff info/ Ruff Mineralogical database.

611   Accessed 15 March 2013

FIGURE CAPTIONS

613 **Figure 1.** Location and geological setting of the San Giovanni Mine, in which

614 the *Crovassa Ricchi in Argento* Cave is located. Light-colored materials

615 represent the carbonate sequence where most of the mine caves in this area

616 are developed. The main geomorphological features of the cave have been

617 represented on the cave topography (after Messina et al., 2005) as well as two

618 cross sections. The location of the corroded calcite crystals and muds subject of

619 this work has been indicated by means of a red star.

620

621 **Figure 2.** Polymetallic oxide crusts and calcite forms on the walls of the upper

622 levels of the *Crovassa Ricchi in Argento* Cave (San Giovanni Mine, SW

623 Sardinia). Planar ochre crusts appear covering the smoothed surface of some

624 crystals and protrude by several centimeters from the cave walls, in particular

625 on the boundaries between calcite crystals, whilst the exposed crystal surfaces

626 appear depressed, showing grey color.

627

628 **Figure 3.** Raman spectra of the minerals in the ochre crust of *Crovassa Ricchi*

629 *in Argento* Cave: A. Binocular microscope image of sample GRA03; B, C and D.

630 Location of the Raman microanalyses: (a) substrate (calcite); (b) dark inclusion

631 (polymetallic oxides, todorokite?); (c) orange ochre inclusion (goethite); (d) dark

632 inclusion (polymetallic oxides, todorokite? + organic substances).

633

634 **Figure 4.** SEM (scanning electron microscope; B, D, E and F) and BSE

635 (backscattered electron; A and C) images showing zones of contrasting

morphologies and compositions. Clearer color zones in Fig. 4A and C indicate

Fe-Mn aggregates while darker color areas are composed of altered calcite

crystals. The lowercase letters (a-e) indicate the locations where the EDX

microanalyses were done (see Table 1).

Table 1. EDX microanalyses (wt.%) of the spots (a-e) located on Fig. 4. Cl, As,

Br and Mg appear below 0.5 wt.%; *carbon is overestimated by 7 wt.% due to

graphite coating (see main text).

Figure 5. Genesis of the reticular ochre crusts of *Crovassa Ricchi in Argento*

Cave: A. Subaqueous precipitation of calcite spars from thermal water. Later,

the water temperature gradually decreased, probably due to an increasing input

of meteoric water to the aquifer; B. Corrosion-dissolution of the crystal surfaces

by colder acid solutions and widening of the spaces between calcite crystals; C.

Deposition of metal-rich clayey sediments on the cave walls and infilling of the

spaces between calcite crystals; D. Partial removal of sediments. Evaporation

and oxygen diffusion into the sediments led to oxide deposition and calcite

corrosion due to acidification; E. Removal of sediments. Simultaneously, the

crusts dehydrated through evaporation. At last calcite corroded due to acidic

condensation waters.